
Robust Learning from Explanations

Juyeon Heo^{*1} Vihari Piratla^{*1} Matthew Wicker² Adrian Weller^{1,2}

Abstract

Machine learning from explanations (MLX) is an approach to learning that uses human-provided annotations of relevant features for each input to ensure that model predictions are *right for the right reasons*. Existing MLX approaches rely heavily on a specific model interpretation approach and require strong parameter regularization to align model and human explanations, leading to sub-optimal performance. We recast MLX as an adversarial robustness problem, where human explanations specify a lower dimensional manifold from which perturbations can be drawn, and show both theoretically and empirically how this approach alleviates the need for strong parameter regularization. We consider various approaches to achieving robustness, leading to improved performance over prior MLX methods. Finally, we combine robustness with an earlier MLX method, yielding state-of-the-art results on both synthetic and real-world benchmarks.

1. Introduction

Deep neural networks (DNNs) display impressive capabilities, making them strong candidates for real-world deployment. However, numerous challenges hinder their adoption in practice. Many of these challenges can be traced back to under-specification or ambiguity in labelled data (D’Amour et al., 2020). For example, standard models were shown to exploit dataset-specific incidental correlations such as the placement of a metal token for diagnosing pneumonia (Zech et al., 2018; DeGrave et al., 2021), or the presence of a patch for diagnosing skin cancer (Codella et al., 2019b). This phenomenon of learning unintended feature-label relationships from examples is referred to as *shortcut learning* (Geirhos et al., 2020). A common suggestion for avoiding shortcut learning is to train on diverse data (Shah et al., 2022) from multiple domains, demographics, etc, but this may be

impractical for many applications such as in healthcare.

On the other hand, additional supervision using human-provided explanations of relevant/irrelevant features in an input is an appealing but under-studied direction towards reducing task under-specification. Learning from human-provided explanations (MLX) has been shown to avoid known shortcuts in the dataset (Schramowski et al., 2020). Ross et al. (2017) pioneered an MLX approach based on regularizing DNNs to ignore features deemed irrelevant by human-provided explanations with the end goal of building models that are “right for the right reasons”, which was followed by several others (Schramowski et al., 2020; Rieger et al., 2020; Stammer et al., 2021; Shao et al., 2021). Broadly, existing approaches employ a model interpretation approach to obtain local feature saliency scores and use these scores to regularize the model such that the feature saliency computed by the tool matches with the human explanation. Since saliency is unbounded for relevant features, many approaches simply regularize the saliency of irrelevant features. Following this line, we typically refer to explanation as a specification of irrelevant features hereafter.

Existing MLX approaches suffer from two critical concerns stemming from their dependence on a local interpretation method. First, their quality of supervision is determined by the nature of the interpretation approaches. While the seminal work of Ross et al. (2017) used gradient-based explanations, Rieger et al. (2020) used a decomposition of relevant and irrelevant features to improve performance, and Shao et al. (2021) advocate for the use of influence functions. The nuances of each local method will impact the effectiveness of reducing shortcut learning, thus making it difficult to select a principled approach to MLX. Second, constraints using local explanations need not apply globally. This is problematic, as we demonstrate both analytically and empirically, as in order for the proposed MLX loss to be globally effective at reducing shortcut learning, heavy parameter regularization is required.

In this work, we systematically study learning from explanations using adversarial robustness methods without depending on external model interpretation tools. We start by framing the provided human explanations as specifications of a local, low-dimensional manifold from which perturbations are drawn. We then notice that a model whose prediction is

^{*}Equal contribution ¹University of Cambridge ²The Alan Turing Institute. Correspondence to: Juyeon heo <jh2324@cam.ac.uk>, Vihari Piratla <vp421@cam.ac.uk>.

invariant to perturbations drawn from the manifold ought to also be robust to irrelevant features (shortcuts). Our perspective yields some considerable advantages. For example, posing MLX as a robustness task enables us to leverage the years of advances in adversarial robustness in order to explicitly train models that are robust to perturbations of irrelevant features. Further, we show in Section 4 that robustness methods can provide upper-bounds on the function deviations to irrelevant feature perturbations if input domain is covered by the training data sufficiently well. Finally, we empirically show that one can get the benefits of both robustness-based and interpretation-based methods by combining them, leading to our proposed algorithm, IBP-Ex+RRR. IBP-Ex+RRR combines an efficient certified robustness algorithm called Interval Bound Propagation (IBP, Gowal et al., 2018) and the simple interpretation based method RRR of Ross et al. (2017). We highlight the following contributions:

- We theoretically and empirically demonstrate that existing MLX methods require strong model regularization owing to their dependence on local model interpretation tools.
- We study learning from explanations using adversarial robustness methods. To the best of our knowledge, we are the first to analytically and empirically evaluate robustness methods for MLX.
- We distill our insights into our proposed algorithm: IBP-Ex+RRR, which consistently yields significant performance gains on two real-world and one synthetic dataset.

2. Problem Definition and Background

We assume access to a training dataset with N training examples, $\mathcal{D}_T = \{(\mathbf{x}^{(i)}, y^{(i)})\}_{i=0}^N$, with $\mathbf{x}^{(i)} \in \mathbb{R}^n$ and $y^{(i)}$ label. Throughout our discussion we assume we have a multi-class classification problem with c classes. In the MLX setting, a human expert specifies input mask $\mathbf{m}^{(n)}$ for an example $\mathbf{x}^{(n)}$ where non-zero values of the mask identify *irrelevant* features of the input $\mathbf{x}^{(n)}$. An input mask is usually designed to negate a known shortcut feature that a classifier is exploiting. Figure 2 shows some examples of masks for the datasets that we used for evaluation. For example, a mask in the ISIC dataset highlights a patch that was found to confound with non-cancerous images. With the added human specification, the augmented dataset contains triplets of example, label and mask, $\mathcal{D}_T = \{(\mathbf{x}^{(i)}, y^{(i)}, \mathbf{m}^{(i)})\}_{i=0}^N$. The task therefore is to learn a model $f(\mathbf{x}; \theta)$ that fits observations well while not exploiting any features that are identified by the mask.

The method of Ross et al. (2017) which we call RRR (Right for the Right Reasons), and also other similar approaches (Shao et al., 2021; Schramowski et al., 2020) employ an explanation algorithm (E) to assign importance scores to input features: $IS(\mathbf{x})$, which is then regularized with a $\mathcal{R}(\theta)$ term such that irrelevant features are not re-

garded as important. Their training loss takes the form shown in Equation 1 for an appropriately defined task-specific loss ℓ .

$$\begin{aligned}
 IS(\mathbf{x}) &= E(\mathbf{x}, f(\mathbf{x}; \theta)). \\
 \mathcal{R}(\theta) &= \sum_{n=1}^N \|IS(\mathbf{x}^{(n)}) \times \mathbf{m}^{(n)}\|^2. \\
 \theta^* &= \arg \min_{\theta} \left\{ \sum_n \ell \left(f(\mathbf{x}^{(n)}; \theta), y^{(n)} \right) \right. \\
 &\quad \left. + \lambda \mathcal{R}(\theta) + \frac{1}{2} \beta \|\theta\|^2 \right\}. \quad (1)
 \end{aligned}$$

CDEP (Rieger et al., 2020) is slightly different, they instead use an explanation method that also takes the mask as an argument to directly estimate the contribution/importance of mask features, which they minimize similarly.

3. Method

Our methodology is built on the interpretation of the provided mask as a specification of a low-dimensional manifold from which input perturbations are drawn. In order to achieve robustness to this class of perturbations we use a min-max optimization approach common in the adversarial robustness literature, but modified for our problem setting:

$$\begin{aligned}
 \theta^* &= \arg \min_{\theta} \sum_n \left\{ \alpha \ell \left(f(\mathbf{x}^{(n)}; \theta), y^{(n)} \right) \right. \\
 &\quad \left. + (1 - \alpha) \max_{\epsilon: \|\epsilon\|_{\infty} \leq \kappa} \ell \left(f(\mathbf{x} + (\epsilon \times \mathbf{m}^{(n)}); \theta), y^{(n)} \right) \right\} \quad (2)
 \end{aligned}$$

We use \times to denote element-wise product throughout. The above formulation uses a weighting α to trade off between the standard task loss, the first term, and the adversarial loss incurred by the neural network being non-robust in the human specified shortcut directions, the second term. We can leverage the many advances in adversarial robustness in order to approximately solve the maximization problem posed in the second half of our loss term. One such approach to solving this maximization would be the straight-forward application of projected gradient descent (PGD) (Madry et al., 2017). Given an input, \mathbf{x} , a mask \mathbf{m} , and a positive value κ , PGD uses a first-order optimization approach to arrive at an input \mathbf{x}^* that approximately solves the maximization in the second term of our loss. We refer to the approach of using PGD in our loss formulation as PGD-Ex. Given the non-convexity of this maximization, however, no guarantees can be made about the quality of the approximate solution \mathbf{x}^* . Reliance on a local attack method in our optimization has the potential to bias our approaches to the specific attack

chosen, as observed in the adversarial robustness literature (Tramer et al., 2020). Both local explanations and local adversarial attacks share this weakness.

An alternative optimization approach that does not admit this weakness is interval bound propagation (IBP) (Gowal et al., 2018). The advantage of IBP over PGD is that it represents a convex relaxation of the non-convex optimization problem. Hence the worst-case returned by IBP is guaranteed to be at least as bad as an attacker could find, and thus represents the worst case performance of the networks w.r.t. the specification. Training using IBP has found remarkable success in a variety of applications (Gowal et al., 2018; Wicker et al., 2022). To adapt this approach to our setting we set the input upper and lower bounds to be $[\mathbf{x}^{(n)} - \kappa \times \mathbf{m}^{(n)}, \mathbf{x}^{(n)} + \kappa \times \mathbf{m}^{(n)}]$. This interval captures all of the points around the input $\mathbf{x}^{(n)}$ such that irrelevant features are perturbed by at most κ and relevant features are left unperturbed. Then, using the method set out in the literature on bound propagation, (Mirman et al., 2018; Gowal et al., 2018), we are able to propagate this interval through the neural network in order to arrive at output upper and lower bounds, denoted $\mathbf{l} \in \mathbb{R}^c$ and $\mathbf{u} \in \mathbb{R}^c$, respectively. Crucially, these upper and lower bounds represent an over-approximate output interval meaning that $\forall \mathbf{x}^* \in [\mathbf{x}^{(n)} - \kappa \times \mathbf{m}^{(n)}, \mathbf{x}^{(n)} + \kappa \times \mathbf{m}^{(n)}]$ we have $f(\mathbf{x}^*) \in [\mathbf{l}, \mathbf{u}]$. Thus, we know that the output interval $[\mathbf{l}, \mathbf{u}]$ captures all possible model behaviors that can occur by perturbing irrelevant features. Using this knowledge, and the fact that these bounds are differentiable, we can incorporate these bounds into our proposed objective:

$$\begin{aligned} \mathbf{l}, \mathbf{u} &= IBP(f(\theta), [\mathbf{x}^{(n)} - \kappa \times \mathbf{m}^{(n)}, \mathbf{x}^{(n)} + \kappa \times \mathbf{m}^{(n)}]) \\ \theta^* &= \arg \min_{\theta} \sum_n \alpha \ell(f(\mathbf{x}^{(n)}; \theta), y^{(n)}) \\ &\quad + (1 - \alpha) \ell(\tilde{f}(\mathbf{x}^{(n)}, y^{(n)}, \mathbf{l}, \mathbf{u}; \theta), y^{(n)}) \end{aligned} \quad (3)$$

where $\tilde{f}(\mathbf{x}^{(n)}, y^{(n)}, \mathbf{l}, \mathbf{u}; \theta) = \mathbf{l} \times \bar{\mathbf{y}}^{(n)} + \mathbf{u} \times (\mathbf{1} - \bar{\mathbf{y}}^{(n)})$.

We use $\bar{\mathbf{y}}^{(n)} \in \{0, 1\}^c$ to denote the one-hot transformation of the label $y^{(n)}$. We refer to this version of the loss as IBP-Ex. Before a theoretical analysis of this loss function, we highlight that a key shortcoming of IBP in previous applications is its inability to scale to large neural networks or high-dimensional domains. However, in our setting, given that only non-salient features can be manipulated, it is intuitive that IBP-Ex would not suffer the same scalability limitations of related IBP-based approaches as long as the the number of irrelevant features remains relatively small. In practice, we observed better convergence when gradually increasing the ϵ -ball around the input (as suggested in (Gowal et al., 2018)), so we start training with a small ϵ . Because of this, we risk learning shortcut features in the beginning that are hard to unlearn later. Hence, to help guide learning when ϵ is small, we saw advantage in combining

IBP-Ex with RRR to even greater effect, which yields our final proposal, denoted as IBP-Ex+RRR, with the following form (where all terms are as defined as above):

$$\begin{aligned} \theta^* &= \arg \min_{\theta} \sum_n \alpha \ell(f(\mathbf{x}^{(n)}; \theta), y^{(n)}) \\ &\quad + (1 - \alpha) \ell(\tilde{f}(\mathbf{x}^{(n)}, y^{(n)}, \mathbf{l}, \mathbf{u}; \theta), y^{(n)}) + \lambda \mathcal{R}(\theta). \end{aligned} \quad (4)$$

In Section 5.2, we analyze on a synthetic dataset the complementary strengths of IBP-Ex and RRR.

4. Theoretical Motivation

In this section, we motivate the merits of robustness-based supervision through nonparametric model analysis on two dimensional data. We argue that supervision using locally-linear explanation methods are insensitive to irrelevant feature perturbations only when the fitted function is sufficiently smoothed, thereby potentially compromising accuracy for robustness. On the other hand, we show that supervision using robustness methods such as IBP-Ex do not require any parameter regularization.

Consider a two-dimensional regression task, i.e. $\mathbf{x}^{(n)} \in \mathcal{X}$ and $y \in \mathbb{R}$. Assume that the second feature is the shortcut that the model should not use for prediction, and denote by $x_j^{(n)}$ the j^{th} dimension of n^{th} point. We infer a regression function f from a Gaussian process prior $f \sim GP(f; 0, K)$ with a squared exponential kernel where $k(x, \tilde{x}) = \exp(-\sum_i \frac{1}{2} \frac{(x_i - \tilde{x}_i)^2}{\theta_i^2})$. As a result, we have two hyperparameters θ_1, θ_2 , which are length scale parameters for the first and second dimensions respectively.

An appealing property of GPs is that we can accommodate any observation on transformed function values as long as the transformation is closed under linear operation (Hennig et al., 2022) (see Chapter 4). Therefore, we can accommodate the regularization with an explanation algorithm as additional supervision: $\{\mathbf{x}^{(n)}, IS(\mathbf{x}^{(n)})\}_n$ if the importance scorer is linear, i.e. $IS(\alpha_1 \mathbf{x}_1 + \alpha_2 \mathbf{x}_2) = \alpha_1 IS(\mathbf{x}_1) + \alpha_2 IS(\mathbf{x}_2)$. For instance, the gradient based or LIME-estimated saliency scores are linear.¹ We specifically analyse the more popular gradient-based saliency score below. We will revise the observations y to include the N partial derivative observations toward the end and denote it by \hat{y} , similarly the kernel K is revised to \hat{K} (the specific form of \hat{K} is in the Appendix A).

The posterior value of the function at an arbitrary point \mathbf{x} would then be of the form $p(f(\mathbf{x}) | \mathcal{D}) \sim \mathcal{N}(f(\mathbf{x}); m_x, k_x)$ where m_x and k_x are appropriately defined posterior mean and variance at \mathbf{x} . The following theorem derives the lower bound on function deviations to nuisance feature pertur-

¹https://en.wikipedia.org/wiki/Linearity_of_differentiation

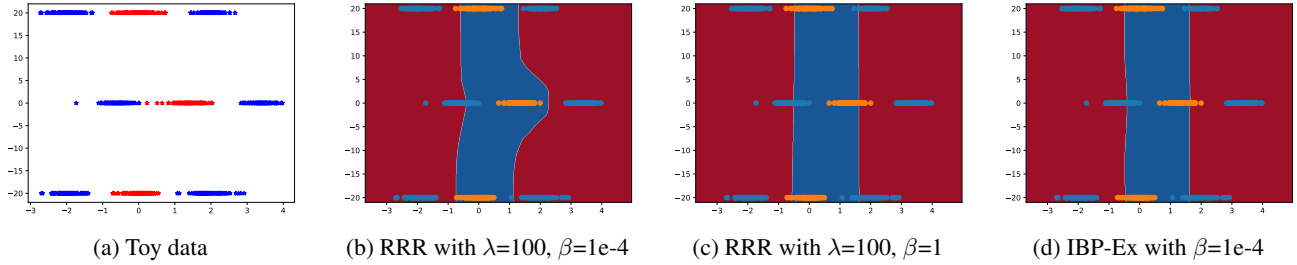


Figure 1. Illustration of the uneasy relationship between RRR and regularization strength. (b) The decision boundary is nearly vertical (zero gradient wrt to nuisance y-axis value) for all training points and yet varies as a function of y value when fitted using unregularized RRR. (c) RRR requires strong model regularization in order to translate local insensitivity to global robustness to vertical value. (d) IBP-Ex fits vertical pair of lines without any model regularization.

bations where the function is obtained by posterior mean marginalised over the two parameters. Further, we impose a Gamma prior over the hyperparameters: $\mathcal{G}(\theta_i^{-2}; \alpha, \beta)$.

For brevity, we denote by $d(x, \tilde{x}) = (x - \tilde{x})^2/2$ and \tilde{y}_i is the $i^{(th)}$ component of $\hat{K}_{XX}^{-1} \hat{y}$.

Theorem 1. *Function value deviations to nuisance feature perturbations are lower bounded by a value proportional to the perturbation strength δ as shown below.*

$$\begin{aligned}
 f(x) &\triangleq \mathbb{E}_\theta[m_x] \\
 &= \int \int m_x \mathcal{G}(\theta_1^{-2}; \alpha, \beta) \mathcal{G}(\theta_2^{-2}; \alpha, \beta) d\theta_1^{-2} d\theta_2^{-2} \\
 f(\mathbf{x} + [0, \delta]^T) - f(\mathbf{x}) &\geq \\
 &\frac{2\delta\alpha}{\beta} \sum_n \left(\frac{1}{1 + \frac{d(x_1, x_1^{(n)})}{\beta}} \right)^\alpha \left(\frac{1}{1 + \frac{d(x_2, x_2^{(n)})}{\beta}} \right)^{\alpha+1} \\
 &\left[(\alpha + 1) \tilde{y}_{n+N} \left(\frac{2(x_2 - x_2^{(n)})(x_2 + \delta - x_2^{(n)})}{\beta + d(x_2, x_2^{(n)})} - 1 \right) - \tilde{y}_n \right] \quad (5)
 \end{aligned}$$

The proof of Theorem 1 is in Appendix A. We begin with the observation that the term under the summation in Eqn. 5 need not be zero for an arbitrary point \mathbf{x} . Therefore, if we wish to fit a function that does not respond to perturbations in x_2 , we may set $\frac{\alpha}{\beta}$ to a very small value, which then diminishes the effect of multiplier from Eqn. 5. Since the expectation of gamma distributed inverse-square length parameter is $\mathbb{E}[\theta^{-2}] = \frac{\alpha}{\beta}$, which we wish to set very small, we are, in effect, sampling functions with very large length scale parameter i.e. strongly smooth functions. This result brings us to the intuitive takeaway that local insensitivity to x_2 applies globally only when the underlying family of functions is sufficiently smooth. Therefore, supervision using locally-linear explanation methods is sub-optimal because they engage performance or expressivity of a function with

its robustness to spurious features. We present a similar result for a two-layer feed-forward parametric model with ReLU activations in Appendix C. We show that when parameters are optimized through gradient descent on RRR loss, then the function value deviations to nuisance feature perturbations is bounded by a factor proportional to L_2 norm of the parameters. The result on parametric models too leads us to the same conclusion that we need to control parameter norm in order to bound function value deviations.

One could also argue that we can simply use different priors for different dimensions, which would resolve the over-smoothing issue. However, we do not have access to parameters specific to each dimension in practice and especially with DNNs, therefore only overall smoothness may be imposed such as with parameter norm regularization in Eqn. 1.

We now look at properties of a function fitted using robustness methods and argue that they are more suitable for learning from explanations.

Theorem 2. *When we use an adversarial robustness algorithm to regularize the network, the fitted function has the following property.*

$$|f(\mathbf{x} + [0, \delta]^T) - f(\mathbf{x})| \leq 2C \frac{\alpha}{\beta} \delta_{max} f_{max}, \quad (6)$$

$$\text{where } C = \max_{\mathbf{x} \in \mathcal{X}} \min_{\hat{\mathbf{x}} \in \hat{\mathcal{X}}} |\mathbf{x}_2 - \hat{\mathbf{x}}_2|.$$

δ_{max} and f_{max} are maximum values of Δ_{x_2} and $f(\mathbf{x})$ in the input domain (\mathcal{X}) respectively. $\hat{\mathcal{X}}$ denotes the subset of inputs covered by the robustness method. C therefore captures the maximum gap in coverage of the robustness method for the input domain (\mathcal{X}).

The proof is in Appendix B. The statement shows that the maximum function deviation is upper bounded by a factor proportional to the C -maximum input coverage gap of the robustness method. Since IBP-Ex provides certified robustness along x_2 , C is pushed very close to 0. We can therefore control the maximum function deviation without needing to regress $\frac{\alpha}{\beta}$ (i.e. without over-smoothing).

Overall, our analysis shows that regularizing with locally linear explanation methods need not guarantee robustness to irrelevant features unless the function is strongly smoothed. On the other hand, regularizing a model with an adversarial robustness method can directly upper bound the sensitivity to irrelevant features without compromising the model expressivity.

Demonstration with simple data. For empirical verification of our results, we fit a classifier with different algorithms using a 3-layer feed-forward network on a two-dimensional data shown in Figure 1 (a), where color indicates the label. We consider fitting a model that is robust to changes in the second feature shown on Y axis. In Figures 1 (b), (c), we show the RRR fitted classifier using gradient ($\partial f / \partial x_2$ for our case) regularization for two different strengths of weight regularization (1e-4 and 1 respectively). With weak regularization, we observe that the fitted classifier is locally vertical (zero gradient along y-axis), but curved overall. With strong regularization, the fitted decision boundary is nearly vertical. However, in practice, strong parameter regularization may excessively limit the model expressivity and may compromise accuracy. On the other hand, IBP-Ex fitted classifier is nearly vertical without any parameter regularization as shown in (d). This example illustrates the need for strong regularization when using a local explanation method.

We empirically observed that the term $\mathcal{R}(\theta)$ (of Eqn. 1), which supervises explanations, also has a regularization effect on the model when the importance scores (IS) are not well normalized, which is often the case. This is because reducing IS(x) for every feature will also reduce it on irrelevant features. For instance, we observed that RRR had reduced gradient for any input pixel by several fold when compared to ERM although the gradient norm of irrelevant feature is reduced even further (Section 5.2). For this reason, increasing λ usually has the same effect as increasing β (of Eqn. 1).

5. Experiments

We evaluate different methods on three datasets, one synthetic and two real-world. The synthetic dataset is similar to decoy-MNIST of Ross et al. (2017) with induced shortcuts and is presented in Section 5.2. For evaluation on practical tasks, we evaluated on a skin cancer detection task presented in Section 5.3, and a plant phenotyping task in Section 5.4. Both the real world datasets contain a known spurious confounding feature, and were used in the past for evaluation of MLX methods. Figure 2 summarises the three datasets, notice that we additionally require in the training dataset the specification of a mask identifying spurious/nuisance features of the input, which as shown in the figure is the

patch for ISIC dataset, background for plant dataset, and decoy half for decoy-MNIST images.

5.1. Setup

5.1.1. BASELINES

We denote by ERM the simple minimization of cross-entropy loss (using only the first loss term of Equation 1).

Interpretation-based methods. We evaluate against two popular interpretation based methods RRR and CDEP, which were discussed in Section 2. We omit comparison with Shao et al. (2021) that uses influence functions instead of gradient based explanations owing to implementation difficulties and computational concerns in handling Hessians.

Robustness-based methods. Apart from PGD-Ex, IBP-Ex and IBP-Ex+RRR that were described in Section 3, we also evaluate with a baseline where training data is augmented with random perturbations of irrelevant features, which was also discussed in Singla et al. (2022) (CoRM) among other methods. For brevity, we denote by CoRM the simple baseline of augmenting with random perturbations.

5.1.2. METRICS

Avg Acc. Since the two real-world datasets contain imbalanced class populations, we only report accuracy macro-averaged over labels, simply denoted as ‘‘Avg Acc’’.

Wg Acc. We also report the worst accuracy among groups for evaluating the model’s dependence on shortcuts where groups are appropriately defined. Different labels define the groups for decoy-MNIST and plant dataset, which therefore have ten and two groups respectively. In ISIC dataset, different groups are defined by the cross-product of label and presence or absence of the patch. Since patch is only present in non-cancerous images, we have three groups for ISIC. We denote this metric as ‘‘Wg Acc’’, which is a standard metric when evaluating on datasets with shortcut features (Sagawa et al., 2019; Piratla et al., 2021).

5.1.3. TRAINING AND IMPLEMENTATION DETAILS

Data splits. We randomly split available labelled data in to training, validation, and test sets in the ratio of (0.75, 0.1, 0.15) for ISIC and (0.65, 0.1, 0.25) for Plant (similar to Schramowski et al. (2020)). We use the standard train-test splits on MNIST.

Hyperparameters. We picked the learning rate, optimizer, weight decay, and initialization for best performance with ERM baseline on validation data, which are not further tuned for other baselines unless stated otherwise. We picked the best λ for RRR and CDEP from [1, 10, 100, 1000]. Additionally, we also tuned β (weight decay) for RRR from [1e-4, 1e-2, 1, 10]. For CoRM, perturbations were drawn

from 0 mean and σ^2 variance Gaussian noise, where σ was chosen from [0.03, 0.3, 1, 1.5, 2]. In PGD-Ex, the worst perturbation was optimized from ℓ_∞ norm ϵ -ball through seven PGD iterations, where the best ϵ is picked from the range 0.03-5. We did not see much gains when increasing PGD iterations beyond 7, Appendix E contains some results when the number of iterations is varied. In IBP-Ex, we follow the standard procedure of Goyal et al. (2018) to linearly dampen the value of α from 1 to 0.5 and linearly increase the value of ϵ from 0 to ϵ_{max} , where ϵ_{max} is picked from 0.01 to 2. We usually just picked the maximum possible value for ϵ_{max} that converges. For IBP-Ex+RRR, we have the additional hyperparameter λ (Eqn. 4), which we found to be relatively stable and we set it to 1 for all experiments.

Choice of the best model. We picked the best model using the held-out validation data. We then report the performance on test data averaged over three seeds corresponding to the best hyperparameter.

Network details. We use four-layer CNN followed by three-fully connected layers for binary classification on ISIC and plant dataset following the setting in (Zhang et al., 2019), and three-fully connected layers for multi classification on decoy-MNIST dataset. More details about network architectures can be found in Appendix D.

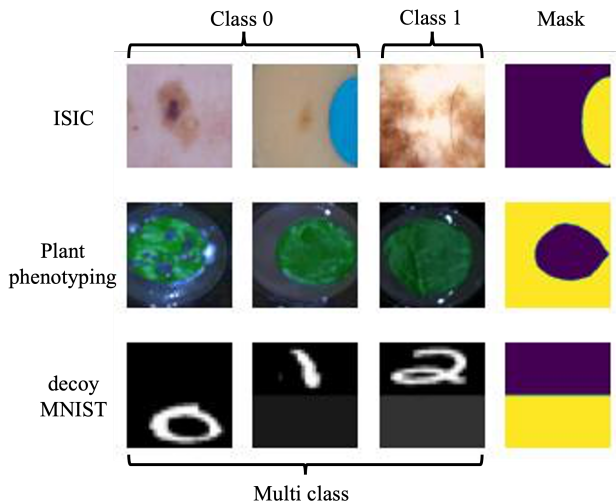


Figure 2. Sample images and masks for different datasets.

5.2. Decoy-MNIST

Our decoy-MNIST dataset is similar to MNIST-CIFAR dataset of Shah et al. (2020) where a very simple label-revealing color based feature (decoy) is juxtaposed with a more complex feature (MNIST image) as shown in Figure 1. We also randomly swap the position of decoy and MNIST parts, which makes ignoring the decoy part more challenging. We then validate and test on images where decoy part

is set to correspond with random other label. See Appendix D for more dataset details.

We make the following observations from the results presented in Table 1. ERM is only slightly better than a random classifier confirming the simplicity bias observed in the past (Shah et al., 2020). Both RRR and IBP-Ex perform better than ERM, but when combined (IBP-Ex+RRR) they perform far better than their individual performance.

In order to understand the surprising gains when using IBP-Ex+RRR, we draw insights from gradients on images from train split for RRR and IBP-Ex. More specifically, we looked at $s_1 = \mathcal{M} \left[\left\| \mathbf{m}^{(n)} \times \frac{\partial f(\mathbf{x}^{(n)})}{\partial \mathbf{x}^{(n)}} \right\| \right]$ and $s_2 = \mathcal{M} \left[\left\| \mathbf{m}^{(n)} \times \frac{\partial f(\mathbf{x}^{(n)})}{\partial \mathbf{x}^{(n)}} \right\| / \left\| (\mathbf{1} - \mathbf{m}^{(n)}) \times \frac{\partial f(\mathbf{x}^{(n)})}{\partial \mathbf{x}^{(n)}} \right\| \right]$, where $\mathcal{M}[\bullet]$ is the median. We expect both s_1, s_2 to be close to zero ideally if the algorithm is successful in fitting a function that does not depend on nuisance features identified by the mask. The values of s_1, s_2 is 2.3e-3, 0.26 for the best model fitted using RRR and 6.7, 0.05 for IBP-Ex. We observe that RRR has lower s_1 while IBP-Ex has lower s_2 , which shows that RRR is good at dampening the contribution of decoy part but that in itself did not increase the contribution of non-decoy. IBP-Ex improves the gradient contribution of the non-decoy part by de-correlating (through random perturbations in ϵ -ball) the decoy part, but did not fully dampen the dependence on decoy part (i.e. $s_1 = 6.7 \gg 0$) due to small initial ϵ as discussed in Section 3. When combined, IBP-Ex+RRR has low s_1, s_2 , which explains the increased performance when they are combined.

Method	Avg Acc	Wg Acc
ERM	15.1 \pm 1.3	10.5 \pm 5.4
RRR	72.5 \pm 1.7	46.2 \pm 1.1
CDEP	14.5 \pm 1.8	10.0 \pm 0.7
CoRM	29.5 \pm 0.3	19.5 \pm 1.4
PGD-Ex	67.6 \pm 1.6	51.4 \pm 0.3
IBP-Ex	68.1 \pm 2.2	47.6 \pm 2.0
IBP-Ex+RRR	96.9 \pm 0.2	95.0 \pm 0.6

Table 1. Average (Avg) and worst group (Wg) accuracy on decoy-MNIST. Results are aggregated from three runs.

5.3. ISIC: Skin Cancer Detection

ISIC is a dataset of cancerous and non-cancerous images of skin lesions, which is to be classified if it is cancerous. Since half the non-cancerous images in the dataset contains a colorful patch as shown in Figure 2, standard DNN models depend on the presence of a patch for classification while compromising the accuracy on non-cancerous images without a patch (Codella et al., 2019a; Tschandl et al., 2018). We follow the standard setup and dataset released by Rieger et al. (2020), which include masks highlighting the patch.

Method	NPNC	PNC	C	Avg	Wg
ERM	55.9	96.5	79.6	77.3	55.9
RRR	67.1	99.0	63.2	76.4	60.2
CDEP	72.1	98.9	62.2	73.4	60.9
CoRM	62.3	97.8	71.0	77.1	55.2
PGD-Ex	65.4	99.0	71.7	78.7	64.4
IBP-Ex	68.4	98.5	67.7	75.1	64.2
IBP-Ex+RRR	66.6	99.6	68.9	78.4	65.2

Table 2. Macro-averaged (Avg) accuracy and worst group (Wg) accuracy on ISIC dataset along with per-group accuracies. All the results are averaged over three runs (see Appendix E for std. dev.).

We identify three groups in the dataset, non-cancerous images without patch (NPNC) and with patch (NCP), and cancerous images (C). In Table 2, we report on models trained for different algorithms, which also includes per-group accuracies along with the usual metrics. The Wg accuracy may not match with the worst of the average group accuracies in the table because we report average of worst accuracies. We now make the following observations. ERM performs the worst on the NPNC group confirming that predictions made by a standard model depend on the patch. The accuracy on the PNC group is high for any algorithm perhaps because PNC group images that contain skin lesions at lower scale (Figure 2, middle column) are systematically more easier to classify irrespective of patch. RRR and CDEP improved NPNC accuracy at the expense of C’s accuracy while still performing relatively poor on Wg accuracy. CoRM performed no better than ERM whereas PGD-Ex, IBP-Ex, and IBP-Ex+RRR significantly improved Wg accuracy over other baselines.

The reduced accuracy gap between NPNC and C for the robustness based methods (except CoRM) is indicative of reduced dependence on patch. Otherwise, if patch is used for prediction then both cancer and non-cancer (without patch) images may be classified as the same class leading to even larger accuracy gap between the two groups. Additional comparisons between PGD-Ex and IBP-Ex can be found in Appendix E.

5.4. Plant Phenotyping

Method	Avg Acc	Wg Acc
ERM	71.3 \pm 2.5	54.8 \pm 1.3
RRR	72.4 \pm 1.3	68.2 \pm 1.4
CDEP	67.9 \pm 10.3	54.2 \pm 24.7
CoRM	76.3 \pm 0.3	64.5 \pm 0.3
PGD-Ex	79.8 \pm 0.3	78.5 \pm 0.3
IBP-Ex	76.6 \pm 3.5	73.8 \pm 1.7
IBP-Ex+RRR	81.7 \pm 0.2	80.1 \pm 0.3

Table 3. Macro-averaged (Avg) accuracy and worst group (Wg) accuracy on Plant phenotyping dataset. All the results are averaged over three runs and their standard deviation is shown after \pm .

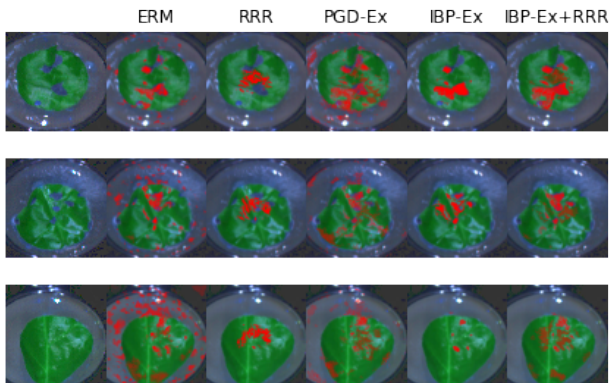


Figure 3. Visual heatmap of salient features for different training algorithms on three sample images from the train split of Plant phenotyping data. Importance score from SmoothGrad (Smilkov et al., 2017) is normalized between 0 to 1 and visualized with a threshold 0.6.

Plant phenotyping is a real-world task of classifying images of a plant leaf as healthy or unhealthy. We study the task using the dataset released by Schramowski et al. (2020), which consists of 1,906 unhealthy leaf images and 504 images of healthy sugar beet plants. Each colored image in the dataset is of size 213 by 213. About half of the diseased leaves show notable signals of the infection called Cercospora Leaf Spot (CLS), which is the black spots on the leaves, as shown in the first image in the second row of Figure 2. However, humans cannot distinguish the other half of them with their eyes since they do not have clear visible CLS, as shown in the second image in second column of Figure 2. Albeit, it is expected that a DNN model can discover useful patterns indicating the leaf infection when present. However, Schramowski et al. (2020) discovered that standard models exploited unrelated features from the nutritional solution in the background in which the leaf is placed, even when clear signs of CLS are visible, thereby performing poorly when evaluated outside of the laboratory setting. Thus, we aim to regulate the model not to focus on the background of the leaf using binary specification masks indicating where the background is located. Due to lack of out-of-distribution test set, we evaluate with in-domain test images but with background pixels replaced by a constant pixel value, which is obtained by averaging over all pixels and images in the training set. We only replace with an average pixel value in order to avoid any undesired confounding from shifts in pixel value distribution. More detailed analysis of the dataset can be found in (Schramowski et al., 2020).

Table 3 contrasts the different algorithms on the plant dataset. All the algorithms except CDEP improve over ERM, which is unsurprising given our test data construction; any algorithm that can divert focus from the background pixels can perform well. Wg accuracy of our three best methods: PGD-

Ex, IBP-Ex and IBP-Ex+RRR far exceed any other method by improving it by 5-12% over the next best baseline and by 19-26% accuracy point over ERM. Surprisingly, even CoRM has significantly improved the performance over ERM perhaps because the volume of informative background features is small enough for even random perturbation to have a good coverage (as defined in Theorem 2).

We visualize the interpretations of models obtained using SmoothGrad (Smilkov et al., 2017) trained with five different methods for three sample images from the train split in Figure 3. As expected, ERM has strong dependence on non-leaf background features. Although RRR features are all on the leaf, they appear to be localized to a small region on the leaf, which is likely due to the regularization effect of its loss. IBP-Ex on the other hand draws features from a wider region and has more diverse pattern of active pixels. Notwithstanding the strong performance, PGD-Ex still depends on background pixels, although much less than ERM. Active regions of IBP-Ex+RRR are scattered well over the leaf and never on the background reaffirming its overall dominance.

5.5. Overall results

Among the interpretation-based methods, RRR performed the best while also being simple and intuitive. However, despite fine-tuning, CDEP failed to improve over ERM on decoy-MNIST and plant datasets. We elaborate more about this finding in Appendix F.

Robustness-based approaches, i.e., PGD-Ex and IBP-Ex, show comparable results to interpretation-based methods on decoy-MNIST, but show notable improvements over interpretation-based methods on real world benchmarks. Specifically, we observe an improvement to W_g accuracy by 3-10% on the two real-world datasets when using robustness-based approaches versus interpretation-based approaches. Surprisingly, PGD-Ex is better than IBP-Ex on all the three datasets despite certified robustness guarantees of IBP-Ex. We reasoned in Section 3 that the relative under-performance of IBP-Ex is due to cold start with small initial ϵ and proposed a light-weight fix of using IBP-Ex+RRR instead. This simple fix to IBP-Ex out-performed all other methods on every dataset while still being 1.4 times faster computationally than PGD-Ex as shown in Table 4.

RRR	PGD-Ex	IBP-Ex	IBP-Ex+RRR
$\times 2.3$	$\times 4.9$	$\times 2.2$	$\times 3.5$

Table 4. Running time in comparison to ERM on the ISIC dataset

6. Related Work

Learning from human-provided explanations Learning from explanations attempts to ensure that model predic-

tions are “right for the right reasons” (Ross et al., 2017). Since gradient-based explanations employed by Ross et al. (2017) are known to be unfaithful (Murphy, 2023) (Chapter 33) (Wicker et al., 2022), subsequent works have proposed to replace the explanation method by a more robust while the overall loss structure remained almost the same. (Shao et al., 2021) proposed to regularize using influence function, while Rieger et al. (2020) proposed to appropriately regularize respective contributions of relevant or irrelevant features to the classification probability through an explanation method proposed in Singh et al. (2018). With a slight departure from these methods, Selvaraju et al. (2019) used a loss objective that penalises ranking inconsistencies between human and model’s salient regions demonstrated for VQA applications. Stammer et al. (2021) argued for going beyond pixel-level importance scores to concept-level scores for the ease of human intervention. On the other hand, Singla et al. (2022) studied performance when augmenting with simple perturbations of irrelevant features and with gradient regularization of Ross et al. (2017). This is the only work, to the best of our knowledge, that explored robustness to perturbations for learning from explanations.

Adversarial Robustness Adversarial examples were first popularized for neural networks in Szegedy et al. (2013), and have been a significant issue for machine learning models for at least a decade (Biggio & Roli, 2018). Local methods for computing adversarial attacks have been studied (Madry et al., 2017), but it is well known that adaptive attacks are stronger (i.e., more readily fool NNs) than general attack methods such as PGD (Tramer et al., 2020). Certification approaches on the otherhand are guaranteed to be worse than any possible attack (Mirman et al., 2018), and training with certification approaches such as IBP have been found to provide state-of-the-art results in terms of provable robustness (Gowal et al., 2018), uncertainty (Wicker et al., 2021), explainability (Wicker et al., 2022), and fairness (Benussi et al., 2022).

7. Conclusions

By casting MLX as an adversarial robustness problem and using human explanations to specify the manifold of perturbations, we have shown that it is possible to alleviate the need for strong parameter regularization of earlier approaches. Borrowing from the well-studied topic of robustness, we evaluated two strong approaches, one from adversarial robustness (PGD-Ex) and one from certified robustness (IBP-Ex). In our evaluation spanning seven methods and three datasets including two real-world datasets we found that PGD-Ex and IBP-Ex performed better than any previous approach, while our final proposal IBP-Ex+RRR of combining IBP-Ex with a light-weight interpretation based method has consistently performed the best without com-

promising compute efficiency. This work represents a step forward in the development of reliable machine learning models.

8. Acknowledgements

MW acknowledges support from Accenture. MW and AW acknowledge support from EPSRC grant EP/V056883/1. AW acknowledges support from a Turing AI Fellowship under grant EP/V025279/1, and the Leverhulme Trust via CFI.

References

- Benussi, E., Patane, A., Wicker, M., Laurenti, L., and Kwiatkowska, M. Individual fairness guarantees for neural networks. *arXiv preprint arXiv:2205.05763*, 2022.
- Biggio, B. and Roli, F. Wild patterns: Ten years after the rise of adversarial machine learning. *Pattern Recognition*, 84:317–331, 2018.
- Codella, N., Rotemberg, V., Tschandl, P., Celebi, M. E., Dusza, S., Gutman, D., Helba, B., Kalloo, A., Liopyris, K., Marchetti, M., et al. Skin lesion analysis toward melanoma detection 2018: A challenge hosted by the international skin imaging collaboration (isic). *arXiv preprint arXiv:1902.03368*, 2019a.
- Codella, N., Rotemberg, V., Tschandl, P., Celebi, M. E., Dusza, S., Gutman, D., Helba, B., Kalloo, A., Liopyris, K., Marchetti, M., et al. Skin lesion analysis toward melanoma detection 2018: A challenge hosted by the international skin imaging collaboration (isic). *arXiv preprint arXiv:1902.03368*, 2019b.
- DeGrave, A. J., Janizek, J. D., and Lee, S.-I. Ai for radiographic covid-19 detection selects shortcuts over signal. *Nature Machine Intelligence*, 3(7):610–619, 2021.
- D’Amour, A., Heller, K., Moldovan, D., Adlam, B., Alipanahi, B., Beutel, A., Chen, C., Deaton, J., Eisenstein, J., Hoffman, M. D., et al. Underspecification presents challenges for credibility in modern machine learning. *Journal of Machine Learning Research*, 2020.
- Geirhos, R., Jacobsen, J.-H., Michaelis, C., Zemel, R., Brendel, W., Bethge, M., and Wichmann, F. A. Shortcut learning in deep neural networks. *Nature Machine Intelligence*, 2(11):665–673, 2020.
- Gowal, S., Dvijotham, K., Stanforth, R., Bunel, R., Qin, C., Uesato, J., Arandjelovic, R., Mann, T., and Kohli, P. On the effectiveness of interval bound propagation for training verifiably robust models. *arXiv preprint arXiv:1810.12715*, 2018.
- Hennig, P., Osborne, M. A., and Kersting, H. P. *Probabilistic Numerics: Computation as Machine Learning*. Cambridge University Press, 2022. doi: 10.1017/9781316681411.
- Madry, A., Makelov, A., Schmidt, L., Tsipras, D., and Vladu, A. Towards deep learning models resistant to adversarial attacks. *arXiv preprint arXiv:1706.06083*, 2017.
- Mirman, M., Gehr, T., and Vechev, M. Differentiable abstract interpretation for provably robust neural networks. In *International Conference on Machine Learning*, pp. 3578–3586. PMLR, 2018.
- Murphy, K. P. *Probabilistic Machine Learning: Advanced Topics*. MIT Press, 2023. URL <http://probml.github.io/book2>.
- Piratla, V., Netrapalli, P., and Sarawagi, S. Focus on the common good: Group distributional robustness follows. *arXiv preprint arXiv:2110.02619*, 2021.
- Rieger, L., Singh, C., Murdoch, W., and Yu, B. Interpretations are useful: penalizing explanations to align neural networks with prior knowledge. In *International conference on machine learning*, pp. 8116–8126. PMLR, 2020.
- Ross, A. S., Hughes, M. C., and Doshi-Velez, F. Right for the right reasons: Training differentiable models by constraining their explanations. *arXiv preprint arXiv:1703.03717*, 2017.
- Sagawa, S., Koh, P. W., Hashimoto, T. B., and Liang, P. Distributionally robust neural networks for group shifts: On the importance of regularization for worst-case generalization. *arXiv preprint arXiv:1911.08731*, 2019.
- Schramowski, P., Stammer, W., Teso, S., Brugger, A., Herbert, F., Shao, X., Luigs, H.-G., Mahlein, A.-K., and Kersting, K. Making deep neural networks right for the right scientific reasons by interacting with their explanations. *Nature Machine Intelligence*, 2(8):476–486, 2020.
- Selvaraju, R. R., Lee, S., Shen, Y., Jin, H., Ghosh, S., Heck, L., Batra, D., and Parikh, D. Taking a hint: Leveraging explanations to make vision and language models more grounded. In *Proceedings of the IEEE/CVF international conference on computer vision*, pp. 2591–2600, 2019.
- Shah, H., Tamuly, K., Raghunathan, A., Jain, P., and Netrapalli, P. The pitfalls of simplicity bias in neural networks. *Advances in Neural Information Processing Systems*, 33: 9573–9585, 2020.
- Shah, R., Varma, V., Kumar, R., Phuong, M., Krakovna, V., Uesato, J., and Kenton, Z. Goal misgeneralization: Why correct specifications aren’t enough for correct goals. *arXiv preprint arXiv:2210.01790*, 2022.

- Shao, X., Skryagin, A., Stammer, W., Schramowski, P., and Kersting, K. Right for better reasons: Training differentiable models by constraining their influence functions. In *Proceedings of the AAAI Conference on Artificial Intelligence*, volume 35, pp. 9533–9540, 2021.
- Singh, C., Murdoch, W. J., and Yu, B. Hierarchical interpretations for neural network predictions. *arXiv preprint arXiv:1806.05337*, 2018.
- Singla, S., Moayeri, M., and Feizi, S. Core risk minimization using salient imagenet. *arXiv preprint arXiv:2203.15566*, 2022.
- Smilkov, D., Thorat, N., Kim, B., Viégas, F., and Wattenberg, M. Smoothgrad: removing noise by adding noise. *arXiv preprint arXiv:1706.03825*, 2017.
- Stammer, W., Schramowski, P., and Kersting, K. Right for the right concept: Revising neuro-symbolic concepts by interacting with their explanations. In *Proceedings of the IEEE/CVF Conference on Computer Vision and Pattern Recognition*, pp. 3619–3629, 2021.
- Szegedy, C., Zaremba, W., Sutskever, I., Bruna, J., Erhan, D., Goodfellow, I., and Fergus, R. Intriguing properties of neural networks. *arXiv preprint arXiv:1312.6199*, 2013.
- Tramer, F., Carlini, N., Brendel, W., and Madry, A. On adaptive attacks to adversarial example defenses. *Advances in Neural Information Processing Systems*, 33:1633–1645, 2020.
- Tschandl, P., Rosendahl, C., and Kittler, H. The ham10000 dataset, a large collection of multi-source dermatoscopic images of common pigmented skin lesions. *Scientific data*, 5(1):1–9, 2018.
- Wicker, M., Laurenti, L., Patane, A., Chen, Z., Zhang, Z., and Kwiatkowska, M. Bayesian inference with certifiable adversarial robustness. In *International Conference on Artificial Intelligence and Statistics*, pp. 2431–2439. PMLR, 2021.
- Wicker, M., Heo, J., Costabello, L., and Weller, A. Robust explanation constraints for neural networks. *arXiv preprint arXiv:2212.08507*, 2022.
- Zech, J. R., Badgeley, M. A., Liu, M., Costa, A. B., Titano, J. J., and Oermann, E. K. Variable generalization performance of a deep learning model to detect pneumonia in chest radiographs: a cross-sectional study. *PLoS medicine*, 15(11):e1002683, 2018.
- Zhang, H., Chen, H., Xiao, C., Gowal, S., Stanforth, R., Li, B., Boning, D., and Hsieh, C.-J. Towards stable and efficient training of verifiably robust neural networks. *arXiv preprint arXiv:1906.06316*, 2019.

A. Proof of Theorem 1

We restate the result of Theorem 1 for clarity.

The posterior mean of the function estimates marginalised over hyperparameters with Gamma prior has the following closed form.

$$\begin{aligned}
 f(x) &\triangleq \mathbb{E}_\theta[m_x] = \int \int m_x \mathcal{G}(\theta_1^{-2}; \alpha, \beta) \mathcal{G}(\theta_2^{-2}; \alpha, \beta) d\theta_1^{-2} d\theta_2^{-2} \\
 f(\mathbf{x}) &= \sum_{n=1}^N \left(\frac{1}{1 + \frac{d(x_1, x_1^{(n)})}{\beta}} \right)^\alpha \left(\frac{1}{1 + \frac{d(x_2, x_2^{(n)})}{\beta}} \right)^\alpha \left[\tilde{y}^{(n)} + \frac{\frac{\alpha}{\beta}(x_2 - x_2^{(n)})}{1 + \frac{d(x_2, x_2^{(n)})}{\beta}} \tilde{y}^{(n+N)} \right] \\
 f(\mathbf{x} + [0, \delta]^T) - f(\mathbf{x}) &\geq \delta \sum_{n=1}^N \left[\alpha \tilde{y}^{(n)} - \frac{(\alpha + 1) \tilde{y}^{(n+N)}}{1 + \frac{d(x_2, x_2^{(n)})}{\beta}} \right]
 \end{aligned}$$

Proof. We first derive the augmented set of observations (\hat{y}) and \hat{K} explained in the main section.

$$\begin{aligned}
 \hat{y} &= [y_1, y_2, \dots, y_N, \partial f(\mathbf{x}^{(1)})/\partial x_2, \partial f(\mathbf{x}^{(2)})/\partial x_2, \dots, \partial f(\mathbf{x}^{(N)})/\partial x_2]^T \\
 k(x^{(i)}, x^{(j)}) &= \begin{cases} \exp(-\frac{1}{2} \sum_{k=1}^2 \frac{(x_k^{(i)} - x_k^{(j)})^2}{\theta_k^2}) & \text{when } i, j \leq N \\ \frac{(x_2^{(i)} - x_2^{(j)})}{\theta_2^2} \exp(-\frac{1}{2} \sum_{k=1}^2 \frac{(x_k^{(i)} - x_k^{(j)})^2}{\theta_k^2}) & \text{when } i \leq N, j > N \\ -\frac{(x_2^{(i)} - x_2^{(j)})}{\theta_2^2} \exp(-\frac{1}{2} \sum_{k=1}^2 \frac{(x_k^{(i)} - x_k^{(j)})^2}{\theta_k^2}) & \text{when } j \leq N, i > N \\ -2 \frac{(x_2^{(i)} - x_2^{(j)})^2}{\theta_2^4} \exp(-\frac{1}{2} \sum_{k=1}^2 \frac{(x_k^{(i)} - x_k^{(j)})^2}{\theta_k^2}) + \frac{1}{\theta_2^2} \exp(-\frac{1}{2} \sum_{k=1}^2 \frac{(x_k^{(i)} - x_k^{(j)})^2}{\theta_k^2}) & \text{when } i, j > N \end{cases}
 \end{aligned}$$

These results follow directly from the results on covariance between observations of f and its partial derivative below (Hennig et al., 2022).

$$\begin{aligned}
 \text{cov}(f(x), \frac{\partial f(\tilde{x})}{\partial \tilde{x}}) &= \frac{\partial k(x, \tilde{x})}{\partial \tilde{x}} \\
 \text{cov}(\frac{\partial f(x)}{\partial x}, \frac{\partial f(\tilde{x})}{\partial \tilde{x}}) &= \frac{\partial^2 k(x, \tilde{x})}{\partial x \partial \tilde{x}}
 \end{aligned}$$

The posterior value of the function at an arbitrary point \mathbf{x} would then be of the form $p(f(\mathbf{x}) | \mathcal{D}) \sim \mathcal{N}(f(\mathbf{x}); m_x, k_x)$ where m_x and k_x are have the following closed form for Gaussian prior and Gaussian likelihood in our case.

$$\begin{aligned}
 m_x &= k(x, X) K_{XX}^{-1} \hat{y} \\
 k_x &= k(x, x) - k(x, X) K_{XX}^{-1} k(X, x)
 \end{aligned}$$

Since m_x, k_x are functions of the parameters θ_1, θ_2 , we obtain the closed form for posterior mean by imposing a Gamma prior over the two parameters. For brevity, we denote by $d(x, \tilde{x}) = (x - \tilde{x})^2/2$ and $\tilde{y}^{(i)}$ is the i^{th} component of $\hat{K}_{XX}^{-1} \hat{y}$.

$$\begin{aligned}
 f(x) &\triangleq \mathbb{E}_\theta[m_x] = \int \int m_x \mathcal{G}(\theta_1^{-2}; \alpha, \beta) \mathcal{G}(\theta_2^{-2}; \alpha, \beta) d\theta_1^{-2} d\theta_2^{-2} \\
 &= \int \int \left[\sum_{n=1}^N k(x, x^{(n)}) \tilde{y}_n + \sum_{n=1}^N \frac{(x_2 - x_2^{(n)})}{\theta_2^2} k(x, x^{(n)}) \tilde{y}_{n+N} \right] \mathcal{G}(\theta_1^{-2}; \alpha, \beta) \mathcal{G}(\theta_2^{-2}; \alpha, \beta) d\theta_1^{-2} d\theta_2^{-2}
 \end{aligned}$$

$$\begin{aligned}
 & \int \int k(\mathbf{x}, \mathbf{x}^{(n)}) \tilde{y}_n \mathcal{G}(\theta_1^{-2}; \alpha, \beta) \mathcal{G}(\theta_2^{-2}; \alpha, \beta) d\theta_1^{-2} d\theta_2^{-2} \\
 &= \int \int \exp\left(-\frac{\theta_1^{-2}(x_1 - x_1^{(n)})^2}{2} + \frac{\theta_2^{-2}(x_2 - x_2^{(n)})^2}{2}\right) \frac{\beta^\alpha}{\Gamma(\alpha)} \theta_1^{-2\alpha+2} \exp(-\beta\theta_1^{-2}) \frac{\beta^\alpha}{\Gamma(\alpha)} \theta_2^{-2\alpha+2} \exp(-\beta\theta_2^{-2}) \tilde{y}_n d\theta_1^{-2} d\theta_2^{-2} \\
 &= \left(\frac{\beta}{\beta + \frac{(x_1 - x_1^{(n)})^2}{2}}\right)^\alpha \left(\frac{\beta}{\beta + \frac{(x_2 - x_2^{(n)})^2}{2}}\right)^\alpha \tilde{y}_n
 \end{aligned}$$

$$\begin{aligned}
 & \int \int \frac{x_2 - x_2^{(n)}}{\theta_2^2} k(\mathbf{x}, \mathbf{x}^{(n)}) \tilde{y}_{n+N} \mathcal{G}(\theta_1^{-2}; \alpha, \beta) \mathcal{G}(\theta_2^{-2}; \alpha, \beta) d\theta_1^{-2} d\theta_2^{-2} \\
 &= (x_2 - x_2^{(n)}) \left(\frac{\beta}{\beta + \frac{(x_1 - x_1^{(n)})^2}{2}}\right)^\alpha \frac{\beta^\alpha / \Gamma(\alpha)}{(\beta + \frac{(x_2 - x_2^{(n)})^2}{2})^{\alpha+1} / \Gamma(\alpha+1)} \tilde{y}_{n+N} \\
 &= \left(\frac{\beta}{\beta + \frac{(x_1 - x_1^{(n)})^2}{2}}\right)^\alpha \frac{\alpha(x_2 - x_2^{(n)})}{\beta + \frac{(x_2 - x_2^{(n)})^2}{2}} \left(\frac{\beta}{\beta + \frac{(x_2 - x_2^{(n)})^2}{2}}\right)^\alpha \tilde{y}_{n+N}
 \end{aligned}$$

Overall, we have the following result.

$$f(x) = \sum_{n=1}^N \left(\frac{1}{1 + \frac{d(x_1, x_1^{(n)})}{\beta}}\right)^\alpha \left(\frac{1}{1 + \frac{d(x_2, x_2^{(n)})}{\beta}}\right)^\alpha \left[\tilde{y}_n + \frac{\frac{\alpha}{\beta}(x_2 - x_2^{(n)})}{1 + \frac{d(x_2, x_2^{(n)})}{\beta}} \tilde{y}_{n+N} \right]$$

We now derive the sensitivity to perturbations on the second dimension.

$$\begin{aligned}
 f(\mathbf{x} + \Delta \mathbf{x}) - f(\mathbf{x}) &= \sum_{n=1}^N \left(\frac{1}{1 + \frac{d(x_1, x_1^{(n)})}{\beta}}\right)^\alpha \left\{ \left[\left(\frac{1}{1 + \frac{d(x_2 + \delta, x_2^{(n)})}{\beta}}\right)^\alpha - \left(\frac{1}{1 + \frac{d(x_2, x_2^{(n)})}{\beta}}\right)^\alpha \right] \tilde{y}_n \right. \\
 &\quad \left. \left[\frac{\frac{\alpha}{\beta}(x_2 + \delta - x_2^{(n)})}{(1 + \frac{d(x_2 + \delta, x_2^{(n)})}{\beta})^{\alpha+1}} - \frac{\frac{\alpha}{\beta}(x_2 - x_2^{(n)})}{(1 + \frac{d(x_2, x_2^{(n)})}{\beta})^{\alpha+1}} \right] \tilde{y}_{n+N} \right\} \quad (7)
 \end{aligned}$$

Using Bernoulli inequality, $(1+x)^r \geq 1+rx$ if $r \leq 0$, we derive the following inequalities.

$$\begin{aligned}
 & \left(\frac{1}{1 + \frac{d(x_2 + \delta, x_2^{(n)})}{\beta}}\right)^\alpha - \left(\frac{1}{1 + \frac{d(x_2, x_2^{(n)})}{\beta}}\right)^\alpha \\
 &= \left(\frac{1}{1 + \frac{d(x_2, x_2^{(n)})}{\beta}}\right)^\alpha \left[\left(\frac{\beta + d(x_2, x_2^{(n)})}{\beta + d(x_2 + \delta, x_2^{(n)})}\right)^\alpha - 1 \right] \\
 &\geq \left(\frac{1}{1 + \frac{d(x_2, x_2^{(n)})}{\beta}}\right)^\alpha - \alpha \left[\frac{\beta + d(x_2 + \delta, x_2^{(n)})}{\beta + d(x_2, x_2^{(n)})} - 1 \right] \\
 &= \left(\frac{1}{1 + \frac{d(x_2, x_2^{(n)})}{\beta}}\right)^\alpha \alpha \left[\frac{d(x_2, x_2^{(n)}) - d(x_2 + \delta, x_2^{(n)})}{\beta + d(x_2, x_2^{(n)})} \right]
 \end{aligned}$$

$$\text{Assuming } |x_2 - x_2^{(n)}| \gg \delta \quad \forall n \in [N] \quad (8)$$

$$\approx \left(\frac{1}{1 + \frac{d(x_2, x_2^{(n)})}{\beta}}\right)^\alpha \alpha \left[\frac{-2\delta(x_2 - x_2^{(n)})}{\beta + d(x_2, x_2^{(n)})} \right] \quad (9)$$

Similarly,

$$\begin{aligned}
 & \frac{\frac{\alpha}{\beta}(x_2 + \delta - x_2^{(n)})}{\left(1 + \frac{d(x_2 + \delta, x_2^{(n)})}{\beta}\right)^{\alpha+1}} - \frac{\frac{\alpha}{\beta}(x_2 - x_2^{(n)})}{\left(1 + \frac{d(x_2, x_2^{(n)})}{\beta}\right)^{\alpha+1}} \\
 & \geq \frac{\alpha}{\beta}(x_2 - x_2^{(n)}) \left(\frac{1}{1 + \frac{d(x_2, x_2^{(n)})}{\beta}}\right)^{\alpha+1} (\alpha + 1) \left[\frac{-2\delta(x_2 - x_2^{(n)})}{\beta + d(x_2, x_2^{(n)})}\right] + \frac{\frac{\delta\alpha}{\beta}}{\left(1 + \frac{d(x_2 + \delta, x_2^{(n)})}{\beta}\right)^{\alpha+1}} \\
 & \geq \frac{\alpha}{\beta}(x_2 - x_2^{(n)}) \left(\frac{1}{1 + \frac{d(x_2, x_2^{(n)})}{\beta}}\right)^{\alpha+1} (\alpha + 1) \left[\frac{-2\delta(x_2 - x_2^{(n)})}{\beta + d(x_2, x_2^{(n)})}\right] \\
 & \quad + \frac{\frac{\delta\alpha}{\beta}}{\left(1 + \frac{d(x_2 + \delta, x_2^{(n)})}{\beta}\right)^{\alpha+1}} (\alpha + 1) \left[\frac{-2\delta(x_2 - x_2^{(n)})}{\beta + d(x_2, x_2^{(n)})} + 1\right] \\
 & = \frac{\alpha + 1}{\left(1 + \frac{d(x_2, x_2^{(n)})}{\beta}\right)^{\alpha+1}} \left[\frac{-2\delta(x_2 - x_2^{(n)})^2\alpha/\beta - 2\delta^2\alpha/\beta(x_2 - x_2^{(n)})}{\beta + d(x_2, x_2^{(n)})} + \frac{\delta\alpha}{\beta}\right] \\
 & = \frac{-2\delta\alpha(\alpha + 1)}{\beta\left(1 + \frac{d(x_2, x_2^{(n)})}{\beta}\right)^{\alpha+1}} \left[\frac{-2(x_2 - x_2^{(n)})[x_2 + \delta - x_2^{(n)}]}{\beta + d(x_2, x_2^{(n)})} + 1\right] \tag{10}
 \end{aligned}$$

Using inequalities 9, 10 in Equation 7, we have the following.

$$\begin{aligned}
 f(\mathbf{x} + \Delta\mathbf{x}) - f(\mathbf{x}) & \geq \sum_n \left(\frac{1}{1 + \frac{d(x_1, x_1^{(n)})}{\beta}}\right)^\alpha \left(\frac{1}{1 + \frac{d(x_2, x_2^{(n)})}{\beta}}\right)^\alpha \\
 & \quad \left[\frac{-2\delta\alpha\tilde{y}_n}{\beta + d(x_2, x_2^{(n)})} + \frac{-2\delta\alpha(\alpha + 1)\tilde{y}_{n+N}}{\beta + d(x_2, x_2^{(n)})} \left(\frac{-2(x_2 - x_2^{(n)})[x_2 + \delta - x_2^{(n)}]}{\beta + d(x_2, x_2^{(n)})} + 1\right)\right] \\
 f(\mathbf{x} + \Delta\mathbf{x}) - f(\mathbf{x}) & \geq \frac{2\delta\alpha}{\beta} \sum_n \left(\frac{1}{1 + \frac{d(x_1, x_1^{(n)})}{\beta}}\right)^\alpha \left(\frac{1}{1 + \frac{d(x_2, x_2^{(n)})}{\beta}}\right)^{\alpha+1} \\
 & \quad \left[(\alpha + 1)\tilde{y}_{n+N} \left(\frac{2(x_2 - x_2^{(n)})[x_2 + \delta - x_2^{(n)}]}{\beta + d(x_2, x_2^{(n)})} - 1\right) - \tilde{y}_n\right] \tag{11}
 \end{aligned}$$

□

B. Proof of Theorem 2

We restate the result of Theorem 2 for clarity.

When we use an adversarial robustness algorithm to regularize the network, the fitted function has the following property.

$$|f(\mathbf{x} + [0, \delta]^T) - f(\mathbf{x})| \leq \frac{\alpha}{\beta} \delta_{max} f_{max} C$$

$$\text{where } C = \max_{\mathbf{x} \in \mathcal{X}} \min_{\hat{\mathbf{x}} \in \hat{\mathcal{X}}} |\mathbf{x}_2 - \hat{\mathbf{x}}_2|$$

δ_{max} and f_{max} are maximum value of Δx_2 and $f(\mathbf{x})$ in the input domain (\mathcal{X}) respectively. $\hat{\mathcal{X}}$ denotes the subset of inputs covered by the robustness method. C therefore captures the maximum gap in coverage of the robustness method.

Proof. We begin by estimating the Lipschitz constant of a GP with squared exponential kernel.

$$\begin{aligned} f(\mathbf{x}) &= K_{xX} K_{XX}^{-1} y \\ \frac{\partial f(x)}{\partial x_2} &= \frac{\partial K_{xX} K_{XX}^{-1} y}{\partial x_2} = \tilde{K}_{xX} K_{XX}^{-1} y \\ \text{where } [\tilde{K}_{xX}]_n &= \frac{\partial}{\partial x_2} \exp\left(-\frac{((x_1 - x_1^{(n)})^2 + (x_2 - x_2^{(n)})^2)}{2\theta^2}\right) \\ &= -\frac{(x_2 - x_2^{(n)})}{\theta^2} [K_{xX}]_n \end{aligned}$$

We denote with δ_{max} the maximum deviation of any input from the training points, i.e. we define δ_{max} as $\max_{\mathbf{x} \in \mathcal{X}} \max_{n \in [N]} |x_2 - x_2^{(n)}|$. Also, we denote by f_{max} the maximum function value in the input domain, i.e. $f_{max} \triangleq \max_{\mathbf{x} \in \mathcal{X}} f(\mathbf{x})$. We can then bound the partial derivative wrt second dimension as follows.

$$\frac{\partial f(\mathbf{x})}{\partial x_2} \leq \frac{\delta_{max} f_{max}}{\theta^2} \leq \frac{\delta_{max} f_{max}}{\theta^2}$$

For any arbitrary point \mathbf{x} , the maximum function deviation is upper bounded by the product of maximum slope and maximum distance from the closest point covered by the adversarial distance method.

$$|f([x_1, x_2]^T) - f([x_1, \hat{x}_2]^T)| \leq \frac{\delta_{max} f_{max}}{\theta^2} \max_{\mathbf{x} \in \mathcal{X}} \min_{\hat{\mathbf{x}} \in \mathcal{X}} |x_2 - \hat{x}_2| = \frac{\delta_{max} f_{max}}{\theta^2} C$$

Therefore,

$$|f(\mathbf{x} + [0, \delta]^T) - f(\mathbf{x})| \leq 2 \frac{\delta_{max} f_{max}}{\theta^2} C$$

Marginalising θ^{-2} with the Gamma prior leads to the final form below.

$$|f(\mathbf{x} + [0, \delta]^T) - f(\mathbf{x})| \leq 2C \frac{\alpha}{\beta} \delta_{max} f_{max}$$

□

C. Parametric Model Analysis

In this section we show that a similar result to what is shown for non-parametric models also holds for parametric models. We will analyse the results for a two-layer neural networks with ReLU activations. We consider a more general case of D dimensional input where the first d dimensions identify the spurious features. We wish to fit a function $f: \mathbb{R}^D \rightarrow \mathbb{R}$ such that $f(\mathbf{x})$ is robust to perturbations to the spurious features. We have the following bound when training a model using gradient regularization of Ross et al. (2017).

Proposition 1. *We assume that the model is parameterised as a two-layer network with ReLU activations such that $f(\mathbf{x}) = \sum_j \beta_j \phi(\sum_i w_{ji} x_i + b_j)$ where $\vec{\beta} \in \mathbb{R}^F$, $\vec{w} \in \mathbb{R}^{F \times D}$, $\vec{b} \in \mathbb{R}^F$ are the parameters, and $\phi(z) = \max(z, 0)$ is the ReLU activation. For any function such that gradients wrt to the first d features is exactly zero, i.e. $\frac{\partial f}{\partial x_i} \Big|_{\mathbf{x}_i^{(n)}} = 0 \quad \forall i \in [1, d], n \in [1, N]$, we have the following bound on the function value deviations for input perturbations from a training instance \mathbf{x} : $\tilde{x} - x = \Delta \mathbf{x} = [\Delta \mathbf{x}_{1:d}^T, \mathbf{0}_{d+1:D}^T]^T$.*

$$|f(\tilde{x}) - f(x)| = \Theta((\|\vec{\beta}\|^2 + \|\vec{w}\|_F^2) \|\Delta \mathbf{x}\|) \quad (12)$$

For a two-layer network trained to regularize gradients wrt first d dimensions on training data, the function value deviation from an arbitrary point $\tilde{\mathbf{x}}$ from a training point \mathbf{x} such that $\tilde{\mathbf{x}} - \mathbf{x} = \Delta \mathbf{x} = [\Delta \mathbf{x}_{1:d}^T, \mathbf{0}_{d+1:D}^T]^T$ is bounded as follows.

$$|f(\tilde{x}) - f(x)| = \Theta((\|\vec{\beta}\|^2 + \|\vec{w}\|_F^2) \|\Delta \mathbf{x}\|)$$

Proof. Recall that the function is parameterised using parameters $\vec{w}, \vec{b}, \vec{\beta}$ such that $f(\mathbf{x}) = \sum_j \beta_j \phi(\sum_i w_{ji}x_i + b_j)$ where $\vec{\beta} \in \mathbb{R}^F, \vec{w} \in \mathbb{R}^{F \times D}, \vec{b} \in \mathbb{R}^F$ are the parameters, and $\phi(z) = \max(z, 0)$ is the ReLU activation.

Since we train such that $\frac{\partial f(\mathbf{x})}{\partial x_i} = 0, i \in [1, d]$, we have that $\frac{\partial f(\mathbf{x})}{\partial x_i} = \sum_j \beta_j \hat{\phi}(\sum_i w_{ij}x_i + b_i)w_{ij}$ where $\hat{\phi}(a) = \max(\frac{a}{|a|}, 0)$.

We now bound the variation in the function value for changes in the input when moving from $\mathbf{x} \rightarrow \tilde{\mathbf{x}}$ where \mathbf{x} is an instance from the training data. We define four groups of neurons based on the sign of $\sum_i w_{ji}x_i + b_j$ and $\sum_i w_{ji}\tilde{x}_i + b_j$. g_1 is both positive, g_2 is negative and positive, g_3 is positive and negative, g_4 is both negative. By defining groups, we can omit the ReLU activations as below.

$$\begin{aligned} f(\tilde{\mathbf{x}}) - f(\mathbf{x}) &= \sum_j \beta_j \phi(\sum_i w_{ji}\tilde{x}_i + b_j) - \sum_j \beta_j \phi(\sum_i w_{ji}x_i + b_j) \\ &= \sum_{j \in g_1} \beta_j \sum_i w_{ji}(\tilde{x}_i - x_i) + \sum_{j \in g_2} \beta_j (\sum_i w_{ji}\tilde{x}_i + b_j) - \sum_{j \in g_3} \beta_j (\sum_i w_{ji}x_i + b_j) \\ &= \sum_{j \in g_1} \beta_j \sum_{i=1}^d w_{ji}(\tilde{x}_i - x_i) + \sum_{j \in g_2} \beta_j (\sum_{i=1}^D w_{ji}\tilde{x}_i + b_j) - \sum_{j \in g_3} \beta_j (\sum_{i=1}^D w_{ji}x_i + b_j) \end{aligned}$$

Since we have that $\sum_{j \in g_1 \cup g_3} \beta_j w_{ij} = 0, \forall i \in [1, d]$, we have

$$\begin{aligned} &= \sum_{j \in g_1} \beta_j \sum_{i=1}^d w_{ji}\tilde{x}_i + \sum_{j \in g_2} \beta_j (\sum_{i=1}^d w_{ji}\tilde{x}_i + \sum_{i=d+1}^D w_{ji}x_i + b_j) - \sum_{j \in g_3} \beta_j (\sum_{i=d+1}^D w_{ji}x_i + b_j) \\ &\quad - \underbrace{\sum_{j \in g_1} \beta_j \sum_{i=1}^d w_{ji}x_i - \sum_{j \in g_3} \beta_j \sum_{i=1}^d w_{ji}x_i}_{=\sum_{i=1}^d x_i \sum_{j \in g_1 \cup g_3} \beta_j w_{ji} = 0} \\ &= \sum_{j \in g_1 \cup g_2} \beta_j \sum_{i=1}^d w_{ji}\tilde{x}_i + \sum_{j \in g_2} \beta_j (\sum_{i=d+1}^D w_{ji}x_i + b_j) - \sum_{j \in g_3} \beta_j (\sum_{i=d+1}^D w_{ji}x_i + b_j) \end{aligned}$$

retaining only the terms that depend on $\Delta x = \tilde{x} - x$, the expression is further simplified as a term that grows with $\Delta \mathbf{x}$ and a constant term that depends on the value of \mathbf{x}

$$\begin{aligned} &= \sum_{j \in g_1 \cup g_2} \beta_j \sum_{i=1}^d w_{ji} \Delta x_i + \text{constant} \\ \implies &= \Theta(\|\beta\| \|\vec{w}\|_F \|\Delta \mathbf{x}\|) \quad \text{Cauchy-Schwartz inequality} \\ &= \Theta((\|\beta\|^2 + \|\vec{w}\|_F^2) \|\Delta \mathbf{x}\|) \end{aligned}$$

□

D. Dataset and model architecture details

ISIC dataset The ISIC dataset consists of 2,282 cancerous (C) and 19,372 non-cancerous (NC) skin cancer images of 299 by 299 size, each with a ground-truth diagnostic label. We follow the standard setup and dataset released by [Rieger et al. \(2020\)](#), which included masks with patch segmentations. In half of the NC images, there is a spurious correlation in which colorful patches are only attached next to the lesion. This group is referred to as patch non-cancerous (PNC) and the other half is referred to as not-patched non-cancerous (NPNC) ([Codella et al., 2019a](#)). Since trained models tend to learn easy-to-learn and useful features, they tend to take a shortcut by learning spurious features instead of understanding the desired diagnostic phenomena. Therefore, our goal is to make the model invariant to such colorful patches by providing a human specification mask indicating where they are.

decoy-MNIST dataset The MNIST dataset consists of 70,000 images of handwriting digit from 0 to 9. Each class has about 7,000 images of 28 by 28 size. We use three-fully connected layers for multi classification with 512 hidden dimension and 3 channels.

Model architecture on the decoy-MNIST dataset

```
Sequential(  
  (0): Conv2d(3, 32, kernel_size=(3, 3), stride=(1, 1), padding=(1, 1))  
  (1): ReLU()  
  (2): Conv2d(32, 32, kernel_size=(4, 4), stride=(2, 2), padding=(1, 1))  
  (3): ReLU()  
  (4): Conv2d(32, 64, kernel_size=(3, 3), stride=(1, 1), padding=(1, 1))  
  (5): ReLU()  
  (6): Conv2d(64, 64, kernel_size=(4, 4), stride=(2, 2), padding=(1, 1))  
  (7): ReLU()  
  (8): Flatten(start_dim=1, end_dim=-1)  
  (9): Linear(in_features=200704, out_features=1024, bias=True)  
  (10): ReLU()  
  (11): Linear(in_features=1024, out_features=1024, bias=True)  
  (12): ReLU()  
  (13): Linear(in_features=1024, out_features=2, bias=True)  
)
```

Model architecture on the ISIC dataset

```
Sequential(  
  (0): Flatten(start_dim=1, end_dim=-1)  
  (1): Linear(in_features=2352, out_features=512, bias=True)  
  (2): ReLU()  
  (3): Linear(in_features=512, out_features=512, bias=True)  
  (4): ReLU()  
  (5): Linear(in_features=512, out_features=512, bias=True)  
  (6): ReLU()  
  (7): Linear(in_features=512, out_features=10, bias=True)  
)
```

Model architecture on the Plant phenotyping dataset

```
Sequential(  
  (0): Conv2d(3, 32, kernel_size=(3, 3), stride=(1, 1), padding=(1, 1))  
  (1): ReLU()  
  (2): Conv2d(32, 32, kernel_size=(4, 4), stride=(2, 2), padding=(1, 1))  
  (3): ReLU()  
  (4): Conv2d(32, 64, kernel_size=(3, 3), stride=(1, 1), padding=(1, 1))  
  (5): ReLU()  
  (6): Conv2d(64, 64, kernel_size=(4, 4), stride=(2, 2), padding=(1, 1))  
  (7): ReLU()  
  (8): Flatten(start_dim=1, end_dim=-1)  
  (9): Linear(in_features=200704, out_features=1024, bias=True)  
  (10): ReLU()  
  (11): Linear(in_features=1024, out_features=1024, bias=True)  
  (12): ReLU()  
  (13): Linear(in_features=1024, out_features=2, bias=True)  
)
```


Method	NPNC	PNC	C	Avg	Wg
ERM	55.9 ± 2.3	96.5 ± 2.4	79.6 ± 6.6	77.3 ± 2.4	55.9 ± 2.3
RRR	67.1 ± 4.8	99.0 ± 1.0	63.2 ± 11.3	76.4 ± 2.4	60.2 ± 7.4
CDEP	72.1 ± 5.4	98.9 ± 0.7	62.2 ± 4.7	73.4 ± 1.0	60.9 ± 3.0
CoRM	62.3 ± 11.7	97.8 ± 0.8	71.0 ± 16.7	77.1 ± 2.1	55.2 ± 6.6
PGD-Ex	65.4 ± 5.4	99.0 ± 0.3	71.7 ± 6.7	78.7 ± 0.5	64.4 ± 4.3
IBP-Ex	68.4 ± 3.4	98.5 ± 1.0	67.7 ± 4.8	75.1 ± 1.2	64.2 ± 1.2
IBP-Ex+RRR	66.6 ± 3.1	99.6 ± 0.2	68.9 ± 4.7	78.4 ± 0.5	65.2 ± 1.8

Table 5. Macro-averaged (Avg) accuracy and worst group (Wg) accuracy on ISIC dataset. Also shown are the average precision scores for each of the three groups. All the results are averaged over three runs and their standard deviation is shown after \pm . Note that the worst group for each run can be different.

E. Addition Results

Comparison of PGD-Ex and IBP-Ex It is difficult to compare the worst group accuracy of IBP-Ex (64.2) and PGD-Ex (64.4) due to the comparably high standard deviation of PGD-Ex (4.3). Therefore, we additionally compare the accuracy drop when colorful patches are removed from images in the PNC group in Table 6. We replace the colorful patch of the image with its mean value, making it look like a background skin color. Note that we evaluate the robustness to concept-level perturbations rather than pixel-level perturbations, as our focus is on avoiding spurious concept features rather than robustness to adversarial attacks. Interestingly, the accuracy drops about 17% and 37% in IBP-Ex and PGD-Ex, respectively, showing that IBP-Ex is more robust to concept perturbations. This can be explained by the effectiveness of robustness methods in covering the epsilon ball with the center of each input point defined in a low-dimensional manifold annotated in the human specification mask. IBP guarantees robustness on any possible pixel combination within the epsilon ball while PGD only considers the worst case in the epsilon ball. When the inner maximization to find the PGD attack is non-convex, an inappropriate local worst case is found instead of the global one. Thus, IBP-Ex shows better robustness when spurious concepts are removed, which involves large perturbations on irrelevant parts within the defined epsilon ball. The combined method IBP-Ex+RRR, where RRR compensates for the practical limitations of the training procedure of IBP-Ex, shows about 1% higher worst group accuracy than IBP-Ex alone.

Method	PNC	PNC (Remove patch)
PGD-Ex	99.0 ± 0.3	62.2 ± 17.0
IBP-Ex	98.5 ± 1.0	81.6 ± 16.5
IBP-Ex+RRR	99.6 ± 0.2	82.5 ± 9.5

Table 6. Comparison between robustness based methods. Macro-averaged accuracy and regval loss before and after removing color patch part of images in PNC group on ISIC dataset.

Results of PGD-Ex with different epsilon and iteration number. We experimented with different values of epsilon and iteration numbers on the ISIC and Plant phenotyping datasets. The epsilon values tested were 0.03, 0.3, 1, 3, and 5, and the iteration numbers were 7 and 25. In Figure 4, the results on the ISIC dataset showed that using an iteration of 7 with different epsilon values resulted in stable results, but using an iteration of 25 resulted in unstable worst group accuracy. However, in the Plant phenotyping dataset, we found that both average and worst group accuracy were similar regardless of the epsilon and iteration values used.

F. Discussion on poor CDEP performance

In Table 5, CDEP demonstrates better performance in worst group accuracy compared to ERM on the ISIC dataset. However, it fails to surpass RRR, which contradicts results from previous research in (Rieger et al., 2020) where CDEP was found to perform better than RRR. This discrepancy may be attributed to the fact that (Rieger et al., 2020) used different metrics (F1 and AUC) and employed a pretrained VGG model to estimate the contribution of mask features, whereas in our study we used worst group accuracy and employed a four-layer CNN followed by three fully connected layers without any pretraining. We do not use a pre-trained model for CDEP in order to make a fair comparison to other methods. As a result, CDEP also fails to improve worst group accuracy over ERM on the Plant Phenotyping and Decoy-MNIST datasets. We further illustrate the interpretations of CDEP on the Plant Phenotyping dataset using Smooth Gradient in Figure 5. In comparison to the

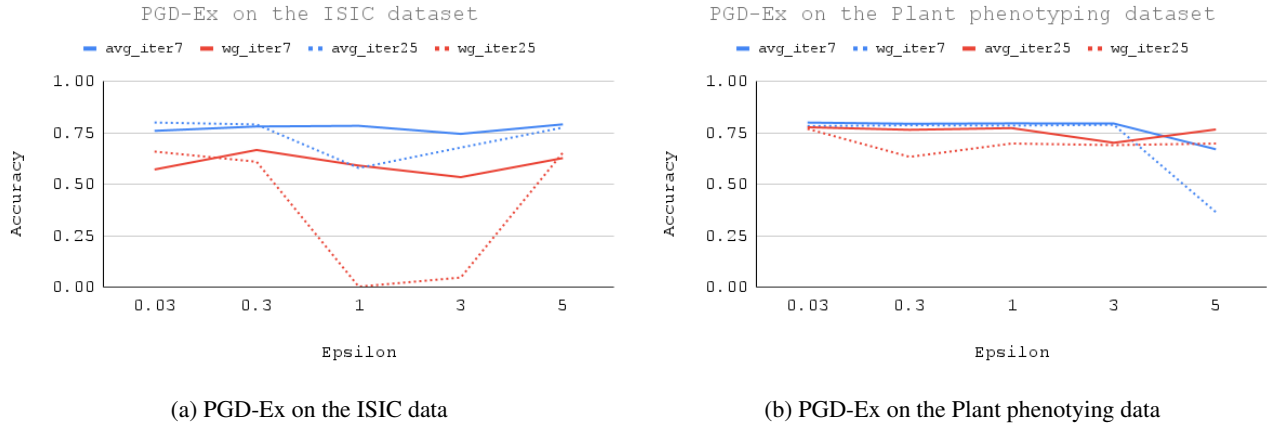


Figure 4. PGD-Ex results on the ISIC and Plant phenotyping dataset with different epsilon and iteration numbers in (a) and (b), respectively.

interpretations of other methods shown in Figure 3 in the main paper, CDEP appears to focus primarily on the spurious agar part instead of the main leaf part.

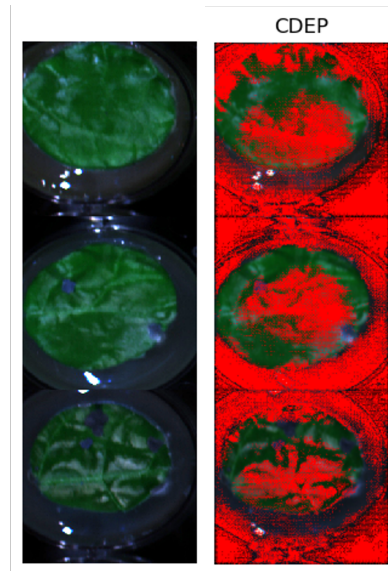


Figure 5. Visual heatmap of salient features for CDEP on three sample images from the train split of Plant phenotyping data. Importance score from SmoothGrad (Smilkov et al., 2017) method is normalized between 0 to 1 and visualized with a threshold 0.6.